ACSNANO

www.acsnano.org

ARTICLE

High-Resolution Shortwave Infrared Imaging of Vascular Disorders Using Gold Nanoclusters

Zhixi Yu, Benjamin Musnier, K. David Wegner, Maxime Henry, Benoit Chovelon, Agnès Desroches-Castan, Arnold Fertin, Ute Resch-Genger, Sabine Bailly, Jean-Luc Coll,* Yves Usson, Véronique Josserand, and Xavier Le Guével*

Cite This: *ACS Nano* 2020, 14, 4973–4981

Read Online

ACCESS | Metrics & More | Article Recommendations | Supporting Information

ABSTRACT: We synthesized a generation of water-soluble, atomically precise gold nanoclusters (Au NCs) with anisotropic surface containing a short dithiol pegylated chain (AuMHA/TDT). The AuMHA/TDT exhibit a high brightness (QY ~ 6%) in the shortwave infrared (SWIR) spectrum with a detection above 1250 nm. Furthermore, they show an extended half-life in blood ($t_{1/2ß}$ = 19.54 ± 0.05 h) and a very weak accumulation in organs. We also developed a non-invasive, whole-body vascular imaging system in the SWIR window with high-resolution, benefiting from a series of Monte Carlo image processing. The imaging process enabled to improve contrast by 1 order of magnitude and enhance the spatial resolution by 59%. After systemic administration of these nanoprobes in mice, we can quantify vessel complexity in depth (>4 mm), allowing to detect very subtle vascular disorders non-invasively in bone morphogenetic protein 9 (*Bmp9*)-deficient mice. The combination of these anisotropic surface charged Au NCs plus an improved SWIR imaging device allows a precise mapping at high-resolution and an in depth understanding of the organization of the vascular network in live animals.

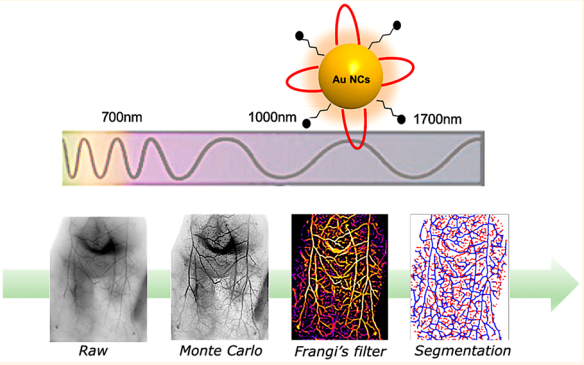

KEYWORDS: *shortwave infrared fluorescence, gold nanoclusters, vascular disorder, Monte Carlo restoration imaging processing, bone morphogenetic protein 9 (Bmp9)*

In the past few years, *in vivo* infrared imaging has experienced major breakthroughs with potential applications in cancer and cardiovascular diagnostics.[1] Hongjie Dai's team developed emitters for the shortwave infrared region (SWIR, 900−1700 nm), also called NIR II. Due to the weak photon absorption, the low autofluorescence, and reduced scattering by tissues at these wavelengths compared to NIR I (700−900 nm) and the visible region, they were able to reach a high spatial and temporal resolution through a few millimeters of tissue, sufficient to image brain blood circulation through the intact skull[2] and in ischemic femoral arteries.[3] Using SWIR imaging, Bawendi *et al.* recently evaluated the metabolic turnover rates of lipoproteins in several organs in real-time as well as the heartbeat and breathing rates in awake and unrestrained animals.[4] Based on these data, they generated a detailed three-dimensional quantitative flow map of the mouse brain vasculature, which demonstrates the high potential of SWIR-imaging applications.

However, only few SWIR-emitting contrast agents are available that possess high quantum yields (QYs), good biocompatibility and low accumulation in organs. Although *in vivo* imaging studies have been performed using SWIR-emitting quantum dots (QDs),[4] the downshifted emission of lanthanide-based nanomaterials,[5] and new organic donor−acceptor−donor (D−A−D)-type organic fluorophores,[6] these materials still have some drawbacks. This includes, for example, their possible toxicity related to the toxicity of their constituents in the case of most QDs and low QYs < 1% for the organic molecules. A relatively new class of NIR II emitters are ultrasmall gold nanoclusters (Au NCs).[7] Recent studies with Au NCs stabilized by zwitterionic sulfobetaine ligands (AuZw) showing a QY of 3.8%, enabled to detect blood vessels using photoluminescence (PL) and revealed efficient renal clearance.[8]

Received: February 10, 2020
Accepted: March 25, 2020
Published: March 25, 2020

https://dx.doi.org/10.1021/acsnano.0c01174
ACS Nano 2020, 14, 4973−4981

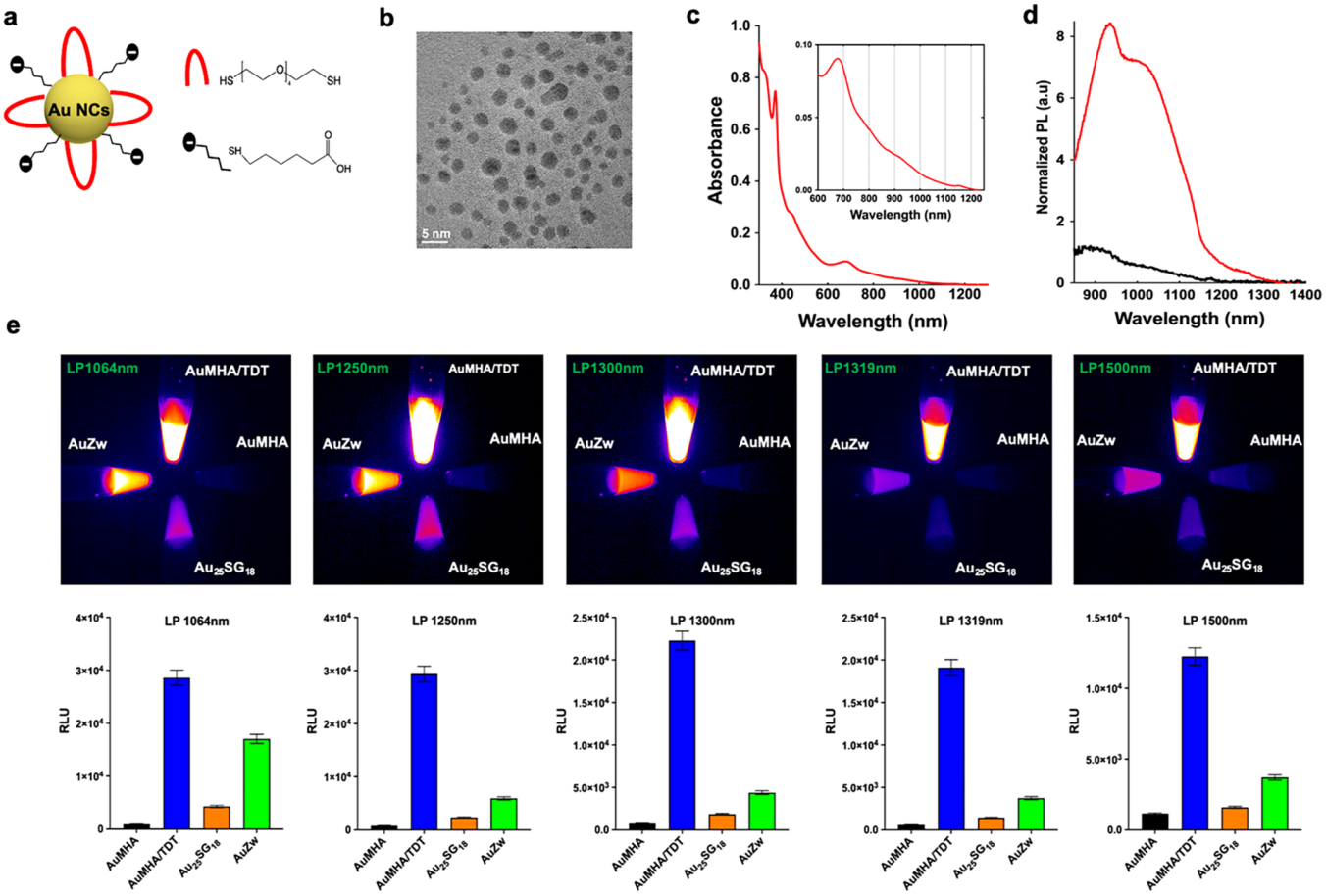

Figure 1. (a) Scheme of the Au NCs AuMHA/TDT (MHA: black; TDT: red). (b) HR-TEM image of AuMHA/TDT. (c) Absorbance spectrum of AuMHA/TDT. (d) PL spectra of AuMHA (black line) and AuMHA/TDT (red line) ($\lambda_{exc.}$ 830 nm). (e) SWIR PL of AuMHA, AuMHA/TDT, $Au_{25}SG_{18}$, and AuZw (300 μM in water) under NIR excitation ($\lambda_{exc.}$ 830 nm) using LP1064 nm (1 ms), LP1250 nm (5 ms), LP1300 nm (10 ms), LP1319 nm (25 ms), and LP1500 nm (250 ms).

In this work, we developed water-soluble Au NCs stabilized by coligands with emission in the SWIR, which exhibit a high brightness, a high photostability, long blood circulation times, and a low toxicity. We demonstrate the ability of this promising contrast agent to image the vascular network of mice with vascular disorders in the second window of the SWIR spectrum (1250−1700 nm) with one-order magnitude contrast enhancement and 59% increase in spatial resolution (x,y). This was enabled by the use of Monte Carlo image processing. The non-invasive image processing, segmentation, and analyses were validated in transgenic mice inactivated for the growth factor *Bmp9* that were previously described with vascular disorders[9,10] based on the measurement of the fractal dimension of vessels.

RESULTS AND DISCUSSION

The here developed Au NCs, named AuMHA/TDT, were prepared by a wet chemistry route using mercaptohexanoic acid (MHA) and tetra(ethylene glycol) dithiol (TDT) as coligands with the molar ratio of Au:ligand = 1:4 and MHA:TDT = 1:3 (Figure 1a, see Materials and Methods). Mass spectrometry revealed a high monodispersity of an 11 kDa species (Figure S1). The average size of the semicrystalline metal core was determined by high-resolution transmission electron microscopy (HR-TEM) to 2.1 ± 0.6 nm (Figures 1b and S2) and the hydrodynamic diameter of AuMHA/TDT in water to 1.90 ± 0.02 nm, as derived from DOSY-NMR (Figure S3). The water-soluble AuMHA/TDT NCs have a negative surface charge at pH 7 of around ζ = −20 mV, which renders them very stable over a long period of time. The addition of the short dithiol molecule TDT on the Au NC surface results in a striking modification of the optical properties, as recently reported by us for another type of anisotropic Au NCs prepared with hexa(ethylene glycol) dithiol as coligand.[11] Indeed, the incorporation of TDT leads to the presence of NIR absorbance features at 800, 910, and 1140 nm (Figure 1c). The anisotropic surface of Au NCs also influences drastically the PL signal in the SWIR region with a 9-fold increase of PL intensity in water accompanied by PL emission at longer wavelengths (Figure 1d). The spectral position and shape of the emission are independent of the excitation wavelength (Figure S4), and the average lifetime derived from the multiexponential decay detected at $\lambda_{em.}$ = 930 ± 20 nm is $\langle\tau_{int.}\rangle$ = 449.0 ns (Figure S5). We compared the PL of AuMHA/TDT to the emission of other water-soluble Au NCs synthesized in our laboratories, that is, AuMHA,[11] AuZw,[12] and $Au_{25}SG_{18}$[13] in different spectral windows in the SWIR. The images in Figure 1e show an up to 12-fold more intense signal for AuMHA/TDT using long pass filters above 1250 nm, confirming the superior brightness of these Au NCs in water as compared to the existing SWIR-emissive ones. We estimated a quantum yield of ∼6%, in the same range as Au NCs stabilized by both ligands

https://dx.doi.org/10.1021/acsnano.0c01174
ACS Nano 2020, 14, 4973−4981

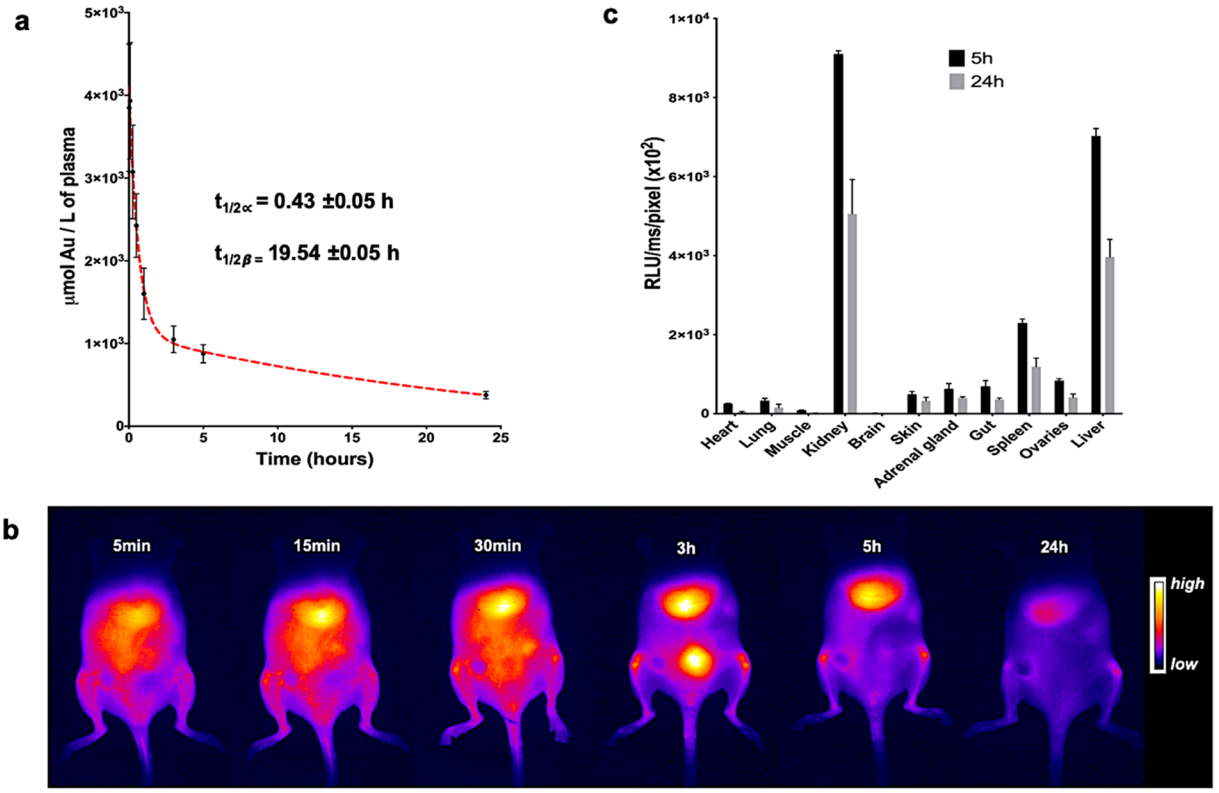

Figure 2. Biodistribution and pharmacokinetics of AuMHA/TDT after intravenous injection in nude mice (360 μM; 200 μL per mouse). (a) *In vivo* pharmacokinetics determined by ICP-MS measurements on plasma samples taken at different time points (n = 4 mice per time points). (b) *In vivo* pharmacokinetic by fluorescence in mice over 24 h ($\lambda_{exc.}$ 830 nm; LP1250 nm). (c) *Ex vivo* 2D fluorescence signal of AuMHA/TDT in isolated organs 5 h and 24 h post-injection (n = 3 mice per time points).

mercaptohexanoic acid (MHA) and dithiol hexa(ethylene glycol) that we previously prepared.[11] This QY is higher than the other Au NCs already in the literature for $Au_{25}SG_{18}$ (0.67%),[14] AuMHA (0.9%),[11] and AuZw (3.8%).[8] The PL features of AuMHA/TDT remain unchanged in water and in the presence of 10% serum (Figure S6). Illumination studies in water, with NaCl (0.9%), and in the presence of bovine serum albumin (BSA; 50 mg/mL) at different incubation times demonstrate the high photostability of these emitters (Figure S7). Surprisingly, in the presence of blood, the PL increases over time. A similar behavior has also been reported for ICG[15] and is tentatively ascribed to specific interactions with proteins/complement components or uptake by red blood cells.

Cytotoxicity experiments (Figure S8) have been conducted using MTT assays with a human embryonic cell line (HEK 293) and human (A549) or murine (4T1) cancer cell lines in the presence of increasing concentrations of AuMHA/TDT up to 45 μM (~500 μg/mL). The absence of significant cell death suggests the low toxicity of these contrast agents and allowed us to move forward to *in vivo* studies.

The half-life of Au NCs in mice is highly dependent on the hydrodynamic diameter of the NCs[12,16] and their density.[17] For instance, small $Au_{25}SG_{18}$ NCs show an extremely fast clearance with a half-life of <2 min as compared to 6 min for the larger AuZw.[12] By elemental analysis (ICP-MS) after AuMHA/TDT administration, we measured a half-life of $t_{1/2\alpha}$ = 0.43 ± 0.05 h and a half-elimination of $t_{1/2\beta}$ = 19.54 ± 0.05 h in nude mice (Figure 2a). These two values are more than 5 times longer than those obtained with the previous applied Au NCs. This prolonged blood circulation time enables the detection of SWIR signals from AuMHA/TDT in the blood vessels in mice up to 30 min after injection. *In vivo* fluorescence measurements also show the renal clearance of these ultrasmall particles with signal in the bladder at 3 h post-injection and with an elimination from the liver observed between 5 and 24 h, respectively (Figure 2b).

One of the major advantages of the SWIR spectral window is the low autofluorescence, which enables to reduce the amount of contrast agent necessary to achieve a high signal-to-noise ratio. In our case, we could detect AuMHA/TDT NCs in *in vitro* samples at concentrations as low as 80 nM with a signal-to-noise ratio of 3.4 (Figure S9). This enabled us to follow the biodistribution of AuMHA/TDT in mice by fluorescence imaging after 5 or 24 h post-injection.

Results from *ex vivo* fluorescence measurements in different organs (Figure 2c), confirmed by ICP-MS measurements (Figure S10), suggest a renal elimination of the Au NCs and an accumulation of the Au NCs mainly in the kidneys, the liver, and the spleen with PL signal dropping by 40% between 5 and 24 h, which suggests an elimination or a metabolization of AuMHA/TDT over time.

Non-invasive real-time SWIR imaging was performed after intravenous injection of AuMHA/TDT (200 μL; 360 μM) *in vivo* in wild-type (WT) mice of the genetic background 129/Ola using a 830 nm laser as light excitation source (50 mW/cm^2) and a long-pass filter LP1250 nm in the emission channel. Under these conditions, the AuMHA/TDT NCs provided a clear and outstanding visualization of the vascular network as shown in Movie S1. As expected, there is a clear improvement of the spatial resolution in the SWIR, which is strongly improved as compared to the NIR I (Figure 3a). We

https://dx.doi.org/10.1021/acsnano.0c01174
ACS Nano 2020, 14, 4973−4981

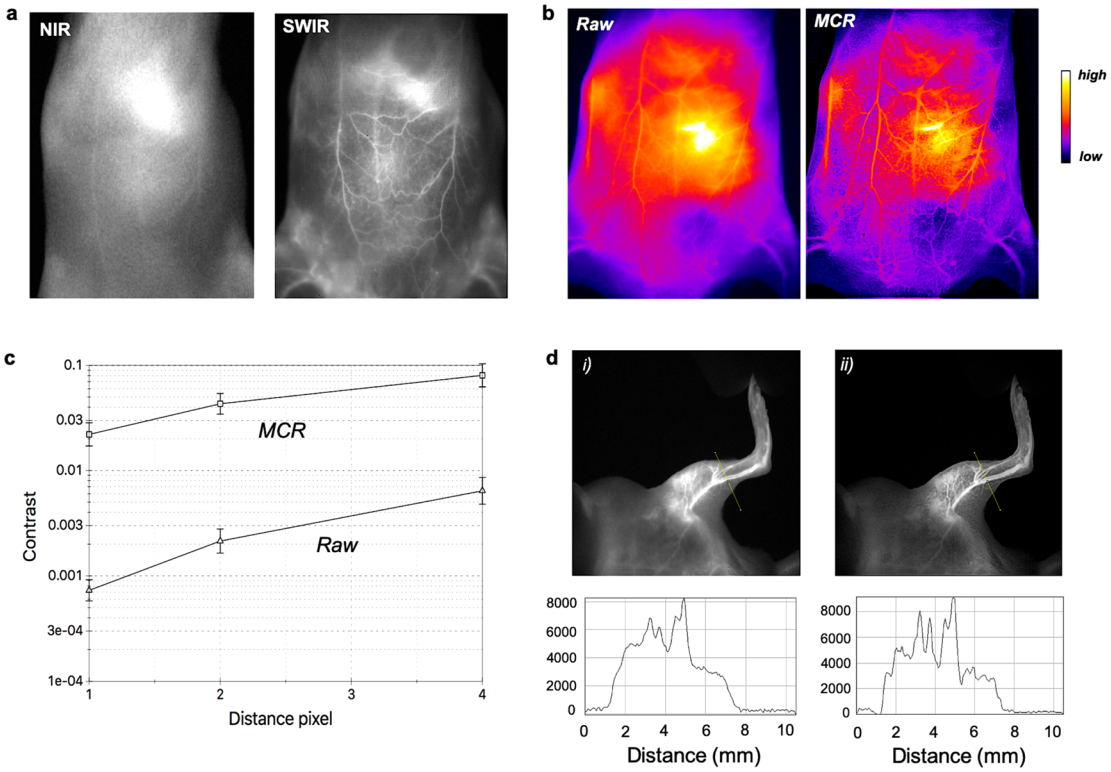

Figure 3. SWIR imaging of blood vasculature in WT 129/Ola mice after intravenous injection of AuMHA/TDT. (a) NIR I ($\lambda_{exc.}$ 780 nm; $\lambda_{em.}$ > 830 nm) and SWIR imaging (LP1250 nm) of mice 15 min after *i.v* injection of AuMHA/TDT (200 μL at 360 μM in PBS). (b) Non-invasive imaging of the mouse ventral area before (raw) and after MCR processing (false colors). (c) Quantification of contrast enhancement per pixel with and without MCR processing on the whole ventral area. (d) Images of the left leg of the mouse (i) before and (ii) after MCR processing with their respective intensity profile across a line of interest drawn in the inset images above.

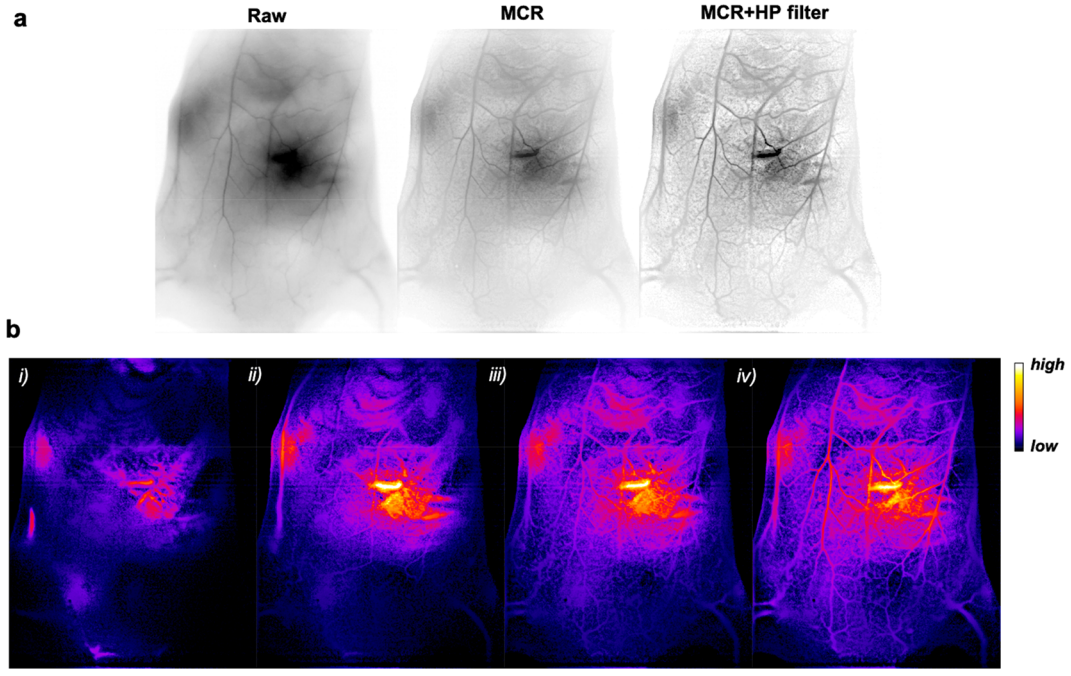

Figure 4. (a) *In vivo* SWIR imaging (reverse contrast) of WT 129/Ola mice vasculature before imaging processing (raw) and after MCR and an additional filtering (MCR + HP filter). (b) MCR + HP filter treated SWIR images (false colors) (i) 1.5 s, (ii) 5 s, (iii) 25 s, and (iv) 65 s after AuMHA/TDT bolus intravenous injection (360 μM; 200 μL).

performed post-image processing with the Monte Carlo constrained restoration (MCR) method to further improve the spatial resolution in depth and to overcome the scattering from the skin and the tissues. Image processing greatly enhances the spatial resolution as seen in Figure 3b. Comparing the quality of the images before and after MCR

https://dx.doi.org/10.1021/acsnano.0c01174
ACS Nano 2020, 14, 4973−4981

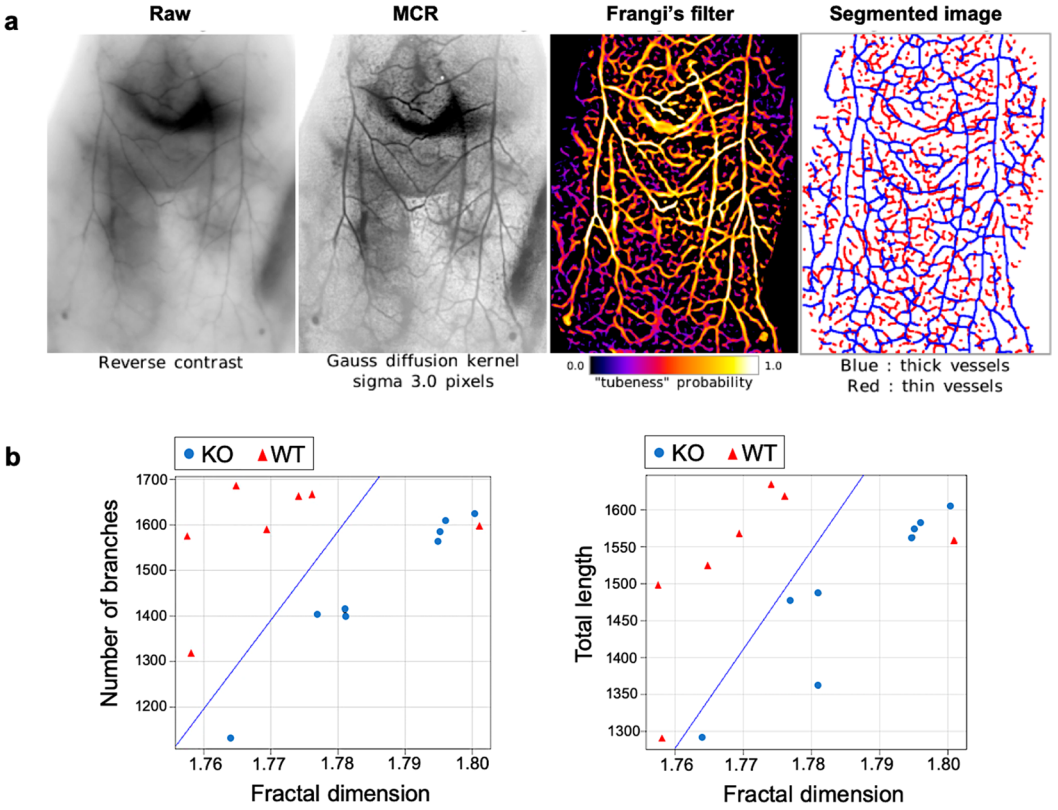

Figure 5. (a) SWIR images of a *Bmp9*-KO mouse after MCR processing, Frangi's filter, and segmentation. (b) Statistical analyses of blood vessel length and branches as a function of fraction dimension performed on *Bmp9*-KO mice (n = 4) and WT mice (n = 4). The blue line highlights the discrimination between the two groups. Each data point is related to a measurement performed on 4 mice but at 1 or 2 different times, which corresponds to 7−8 conditions.

using a quantitative measure of the contrast (Figure 3c) demonstrates an improvement in contrast by 1 order of magnitude, highlighting the potential of this restoration. The determination of the transverse section of blood vessels from the SWIR images of a mouse leg depicted in Figure 3d highlights the excellent resolution after MCR processing and the ability to obtain highly detailed *in vivo* imaging of the whole-body blood vasculature and of the blood brain vasculature (Figure S11). The improvement in resolution reaches 59%, as measured using controlled experimental sets (phantoms) and also by comparing the full width at half-maximum (fwhm) of the vessel peaks on the profiles.

Image processing was then pushed one step further using a high-pass filter to reduce scattering deeper under the skin. Restorations of the first movie by MCR plus the high-pass filter underline the striking improvement of the contrast (Movie S2, Figure S12) allowing the visualization of the vascular network in depth (Figure 4a). After sacrifice of the mice and surgical operation, we evaluated that we were able to detect fluorescent details down to 4 mm below the skin surface. We could also easily track the contrast agent (SWIR-emitting AuMHA/TDT) in mice especially in the first seconds after injection (Movie S3, Figure 4b).

To demonstrate the potential of combining SWIR imaging, image restoration, and image analysis for biomedical applications, non-invasive vascular imaging was performed in mice previously described with vascular disorders due to the inactivation of the gene encoding *Bmp9*[9,10] and compared to WT mice. *Bmp9* has been identified as a high affinity ligand for the endothelial specific receptor activin receptor-like kinase 1 (ALK1) that is mutated in the rare vascular disease hereditary hemorrhagic telangiectasia (HHT).[18] We previously published that genetic deletion of *Bmp9* in the C57BL/6 mouse strain led to lymphatic vascular defects, while it did not affect blood vessels.[19] However, more recently, we found that *Bmp9* deletion in the 129/Ola genetic background led to a much stronger phenotype than in the C7BL/6 strain with premature death and that these mice presented dilated blood liver vessels that ultimately led to liver fibrosis.[9]

To make the proof of concept that AuMHA/TDT would be able to detect vascular disorders, we thus choose to compare WT *versus* *Bmp9*-KO mice of the 129/Ola strain. These mice were placed in the supine position and were injected intravenously with AuMHA/TDT for real-time SWIR imaging from t = 0 to 15 min. MCR was performed on raw images followed by Frangi's filtering and segmentation (see Materials and Methods), as illustrated in Figure 5a. Then, analyses of the segmentation, which provide blood network mapping, were plotted considering the length of the vessels or the number of vessel "branches" (segments delimited by forks or crossings) as a function of the fractal dimension (Figure 5b). Fractal dimension is referred here as the level of complexity of vessels with a numerical value between 1 (straight line tube) and 2 (highly swaying vessel in 2D section). Analyses show a clear distinction in skin vessels between *Bmp9*-KO and WT mice considering both vessel lengths and branches. The significant 4% increase of the fractal dimension for *Bmp9*-KO compared to WT mice, which is correlated to the vessel distortion, confirms the hypothesis of tortuous vessels due to a defect in vessel maturation.[10] Thus, this non-invasive method allowed us

https://dx.doi.org/10.1021/acsnano.0c01174
ACS Nano 2020, 14, 4973−4981

to detect a vascular disorder present in the *Bmp9*-KO mice with such a high level of precision.

CONCLUSION

In conclusion, we report here the design of a bright SWIR-emitting contrast agent with prolonged circulation and efficient elimination that enables the visualization of the vascular network with enhanced-spatial resolution (59%) and contrast (1 order of magnitude) in depth (>4 mm) using a series of MCR processing steps. Both image processing and segmentation analyses enabled to distinguish non-invasively vascular disorders in mice with good confidence. These results, obtained non-invasively, in depth, in real-time, and using whole-body optical imaging, highlight the considerable advantages of combined research on relatively bright contrast agents and on image processing and analyses to improve the sensitivity of SWIR imaging for advanced biomedical applications.

MATERIALS AND METHODS

Matrix-Assisted Laser Desorption Ionization-Time of Flight. Au NCs sample was diluted in the matrix CHCA (α-cyano-4-hydroxy-3-iodocinnamic acid) with 0.1% trifluoroacetic acid in a mixture water/acetonitrile 50/50 v/v. Measurements were performed in positive linear mode on an Autoflex speed instrument from Bruker.

Nuclear Magnetic Resonance (NMR) Spectroscopy. NMR experiments were carried out at 298 K with a Bruker AVANCE III 500 MHz spectrometer equipped with a cryo-probe Prodigy. For each sample the concentration was ~2 mM in D_2O and pH 7. Diffusion ordered NMR spectroscopy (DOSY) experiments were run using the standard "ledbpg2s" Bruker sequence with linear gradient stepped between 2% and 98%. 32 scans were recorded for each gradient step. Data processing was performed using the maximum entropy algorithm from Dynamics Center, a Bruker's NMR software to obtain the diffusion coefficient D. An average value of D was used for the hydrodynamic diameter (HD) calculation according to the Stokes−Einstein equation which assumes that molecules are spherical:

$$\mathrm{HD} = k_B T/3D\pi\eta$$

where k_B is the Boltzmann constant, T is the temperature, η is the viscosity of the solvent (η_{D_2O} = 1.232 10−3 Pa.s at 298 K). Standard one- and two-dimensional (2D) (NOESY, COSY, TOCSY, and HSQC) spectra were recorded using standard presaturation on the water signal.

Zeta Potential. The ζ potentials of Au NCs dispersed in water or in PBS buffer with 10% serum were measured with a Zetasizer from Malvern instruments.

High-Resolution Transmission Electron Microscopy. Metal core sizes were determined by HR-TEM with an 200 kV monochromated TEM using dispersed Au NCs on ultrafine carbon films.

UV−vis-NIR. Absorption spectra of diluted AuNC samples were recorded on a UV−vis-NIR spectrophotometer Cary5000 between 350 and 1700 nm.

Steady-State Photoluminescence. Steady-state PL spectra were measured from 600−1750 nm with a calibrated FSP 920 (Edinburgh Instruments, Edinburgh, United Kingdom) spectrofluorometer equipped with a nitrogen-cooled PMT R5509P.

Time-Resolved Measurements. Measurements were performed in the wavelength region of 930 ± 20 nm using a FLS 920 (Edinburgh Instruments, Edinburgh, United Kingdom) lifetime spectrofluorometer equipped with an EPL-510 (Edinburgh Instruments, Edinburgh, United Kingdom) picosecond pulsed diode laser (excitation wavelength of 510 ± 10 nm; power of 5mW) and a fast PMT R2658P from Hamamatsu, respectively.

Relative Measurements of PL QYs. Measurements of PL QYs ($\Phi_{f,x}$) were performed using the dye IR125 dissolved in dimethyl sulfoxide (DMSO) as reference. The QY of this dye was previously determined absolutely to $\Phi_{f,st}$ = 0.23). The relative QY were calculated according to the formula of Demas and Crosby, see equation below:

$$\Phi_{f,x} = \Phi_{f,st}\frac{F_x}{F_{st}} \times \frac{f_{st}(\lambda_{ex,st})}{f_x(\lambda_{ex,x})} \times \frac{n_x^2(\lambda_{ex,x})}{n_{st}^2(\lambda_{ex,st})}$$

where subscripts x, st, and ex denote sample, standard, and excitation, respectively, $f(\lambda_{exc.})$ is the absorption factor, F the integrated spectral fluorescence photon flux, and n the refractive index of the solvents used (DMSO for IR125; water for Au NCs).

All spectroscopic measurements were done in 1 cm quartz cuvettes from Hellma GmbH at room temperature using air-saturated solutions.

Cytotoxicity Experiments. HEK, 4T1, and A549 cells were seeded in a 96-well plate (5000 cells/well in 100 μL of DMEM with 10% serum) 1 day before the experiment. Au NCs were diluted in DMEM with 10% serum to reach the following final concentrations: 25, 100, 250, and 500 μgAu/mL and added to the cells. Cell viability was evaluated 24 h after Au NCs incubations in triplicate. For positive and negative controls, cells with or without 1 μM staurosporine treatment (cell-death inducer) were also prepared. In order to verify the absence of artifact due to the absorption of the Au NCs, wells with only Au NCs in DMEM with 10% serum were also prepared. Then 20 μL of MTS reagent (Cell-Titer 96, Promega) was added to each well and further incubated at 37 °C for 2 h. The cell density was then determined by the absorbance at 486 nm using a microplate spectrophotometer (Fluostar Omega BM6 LABTECH). The percentages of cell viability were compared using the nonparametric Kruskal−Wallis test. All analyses were performed using GraphPad Prism software. Statistical significance was defined as p values <0.001.

NIR I Imaging. Imaging was performed with a NIR 2D-Fluorescence Reflectance Imaging device (Fluobeam 800, Fluoptics, France). The excitation is provided by a class 1 expanded laser source at 780 nm, and the irradiance on the imaging field is 10 mW/cm^2. The fluorescence signal is collected by a CCD through a high-pass filter with a high transmittance for wavelength >830 nm.

SWIR Imaging. Imaging was performed using a Princeton camera 640ST (900−1700 nm) coupled with a laser excitation source at λ = 830 nm (50 mW/cm^2). We use short-pass excitation filter at 1000 nm (Thorlabs) and long-pass filters on the SWIR camera from Semrock (LP1064 nm, LP1319 nm) and Thorlabs (LP1250 nm, LP1300 nm, LP1500 nm). A 25 mm or 50 mm lense with 1.4 aperture (Navitar) was used to focus on the samples or mice.

Tubes containing AuNC solution and 10 μL drops of each samples were placed in front of the camera using the 50 mm lens and various long pass filters (LP1064 nm, LP1250 nm, LP 1300 nm, LP1319 nm, LP1500 nm). Analyses were performed using FIJI software.

Mice were imaged after intravenous injection (200 μL of Au NCs at 360 μM) using the 25 mm or 50 mm lenses and LP1250 nm at different exposure times (25 ms to 2s). *Ex vivo* fluorescence imaging on isolated organs and plasma samples was performed using the 50 mm lens and LP1064 nm.

Inductively Coupled Plasma-Mass Spectrometry. ICP-MS was performed to determine Au content in organs and in plasma samples at different time point using a Thermo X series II spectrometer (Thermo Electron, Bremen, Germany), which was equipped with an impact bead spray chamber and a standard nebulizer (1 mL·min^{-1}). For sample preparation, the organs and plasma samples were weighted before addition of nitric acid (final concentration 1%), and Au content was determined using an external linear calibration curve (between 10 and 100 μg/L of Au(III)). Indium was used as the internal standard. Determinations were carried out in triplicate.

***In Vivo* Experiments.** For the biodistribution study, 6 week-old NMRI female nude mice (Janvier, France) were anesthetized (air/isoflurane 4% for induction and 1.5% thereafter) and were injected intravenously *via* the tail vein with 200 μL of Au NCs at 360 μM. *In vivo* SWIR fluorescence imaging was performed before and 5 and 24 h

https://dx.doi.org/10.1021/acsnano.0c01174
ACS Nano 2020, 14, 4973−4981

after injection. Mice were euthanized at 5 or 24 h post-injection (n = 3 mice per time point), and organs were harvested for *ex vivo* fluorescence imaging and ICP measurements.

For the pharmacokinetic study, three other mice were injected, and blood samples were collected before and 1, 5, 15, 30, 60, 180, 300, and 1440 min after injection and were centrifuged (10 min at 2000 g) to separate plasma. Plasma pharmacokinetics was obtained from fluorescence imaging and ICP-MS measurements after analyses through a noncompartment model (GraphPad Prism 7.00, GraphPad Software, La Jolla California, USA).

Non-Invasive SWIR Imaging on Mice with Vascular Disorders. Generation of *Bmp9*-KO mice in the 129-P2/Ola-Hsd genetic background (named here for easiness 129/Ola) has been previously described.[9,10] Briefly, *Bmp9*-KO mice in the C57BL/6 genetic background were obtained from Dr. Se-Jin Lee (Johns Hopkins University, Baltimore, MD) and backcrossed for 10 generations with 129-P2/Ola-Hsd WT mice (Harlan France, Gannat, France).

All animal experiments followed the institutional guidelines formulated by the European Community for the Use of Experimental Animals and were approved by ethics committees (CEA ethic committee for animal breeding and Cometh38 for *in vivo* imaging) and the French Ministry of Research and Education (agreement APAFIS no. 9436-2017032916298306 and APAFIS no. 21916-2019082710189095_v4).

Image Restoration of SWIR Fluorescent Images. SWIR already provides stunning fluorescent images *in vivo*, however these images still suffer from light diffusion by the tissues, and the quality of such images can still be improved using image restoration techniques. We used a MCR algorithm based on an original idea by Frieden *et al.*[20] for restoring binary images and then extended to fluorescent image deconvolution by Colicchio *et al.*[21] This algorithm has the advantage of perfectly preserving the amount of information on the image (intensity integral) and achieve powerful contrast and resolution enhancements, while minimizing the ringing artifacts usually encountered with regular iterative constrained deconvolution. However, Monte Carlo algorithms are very computer intensive, and parallelization schemes must be used to speed up calculations.

Assessment of Image Enhancement. The enhancement of fluorescent images was both assessed by visual inspection (qualitative assessment) and by using a quantitative measurement. This was achieved by quantifying the contrast C_d within the image at different positions (distance d = 1, 2, and 4 pixels). The contrast C_d was expressed as the gradient integral of the image.

$$C_d = \frac{\sum_1^{r-d}\sum_1^{c-d}\left(\left(\frac{\delta i}{\delta_d x}\right)^2 + \left(\frac{\delta i}{\delta_d y}\right)^2\right)}{\langle i^2\rangle}$$

with

$$\frac{\delta i}{\delta_d x} = i(x+d, y) - i(x, y); \quad \frac{\delta i}{\delta_d y} = i(x, y+d) - i(x, y);$$

$$\langle i\rangle = \frac{\sum_1^r\sum_1^c i(x, y)}{r \times c}$$

where $i(x,y)$ is the intensity at pixel (x,y), d is the extent of the partial derivate (in pixels), $\delta i/\delta_d x$ is the partial derivate of intensity along x and $\delta i/\delta_d y$ is the partial derivate of intensity along y at pixel (x,y), r is the number of rows, and c is the number of columns in the image.

Vessel Detection and Analysis. The analysis of the vascularization was performed by image analysis of the restored images. We used a classical Frangi's filter that was designed to enhance tubular structures in a gray level image.[22] The advantage of Frangi's filter is a good immunity to noise that reduces overdetection. Frangi's filter provides a "tubeness" or "vesselness" probability image to which a probability threshold can be applied in order to obtain a binary mask of the vascular network. After iterative thinning of the binary mask, a skeleton is obtained, and a neighborhood analysis is applied in order to extract branches, forks, and crossings. The statistical analysis of the various features extracted from the skeleton such as the fractal dimension, total length, the number of branches, the number of forks and crossings and is used to quantify possible differences between mouse strains. The fractal dimension is a mathematical tool which provides a measure of the space-filling capacity of a pattern (here the vascular network). For example, a straight line in a plane has a fractal dimension of one, while a swaying line has a greater fractal dimension (>1 and <2). And as the line gains in complexity and tortuosity, its fractal dimension grows accordingly with a maximum upper limit of 2 that corresponds to the dimension of the plane it is embedded in. Each data point is related to a measurement performed on 4 mice but at 1 or 2 different times, which corresponds to 7−8 conditions.

Synthesis of Au NCs. Chemical products were purchased in Sigma-Aldrich (France), and deionized water was used for all synthesis.

We slightly modified a protocol described by Musnier *et al.*[11] to produce the SWIR-emitted Au NCs using the initial molar ratio Au:ligand = 1:4. Briefly 250 μL of $HAuCl_4{\cdot}3H_2O$ (20 mM) was added to 4.8 mL of water followed by 4 mL of the thiolated ligand mixture mercaptohexanoic acid (MHA, 5 mM))/tetra(ethylene glycol) dithiol (TDT, 5 mM) changing color from yellowish to slightly pale cloudy with a volume ratio MHA/TDT = 3 mL/1 mL. After 5 min, 250 μL of NaOH (1M) was added dropwise leading to almost colorless solutions. After 5 min, 150 μL $NaBH_4$ (20 mM in 0.2 M NaOH) was introduced dropwise under mild stirring and kept under stirring at 350 rpm for 8 h. Purification of the AuMHA/TDT on 3 kDa cutoff filter column (Amicon) was repeated 3 times to stop the reaction, and solutions were kept stored in the fridge before characterization.

The Au NCs, AuMHA,[11] $AuZwMe_2$,[8] and $Au_{25}SG_{18}$[23] were synthesized following the protocols described in the literature.

ASSOCIATED CONTENT

Supporting Information

The Supporting Information is available free of charge at https://pubs.acs.org/doi/10.1021/acsnano.0c01174.

Physicochemical and photophysical of Au NCs, cytotoxicity, and additional *in vivo* experiments in mice (PDF)

Movie S1: *In vivo* SWIR imaging of WT 129/Ola mice vasculature (AVI)

Movie S2: Comparison of *in vivo* SWIR imaging of WT 129/Ola mice vasculature after imaging processing (MCR; MCR + HP filtering) (AVI)

Movie S3: *In vivo* SWIR imaging (MCR + HP filtering) after injection (AVI)

AUTHOR INFORMATION

Corresponding Authors

Xavier Le Guével − *Cancer Targets and Experimental Therapeutics, Institute for Advanced Biosciences (IAB), University of Grenoble Alpes (UGA)/ INSERM-U1209/ CNRS-UMR 5309, 38700 Grenoble, France;* orcid.org/0000-0003-3634-7762; Email: xavier.le-guevel@univ-grenoble-alpes.fr

Jean-Luc Coll − *Cancer Targets and Experimental Therapeutics, Institute for Advanced Biosciences (IAB), University of Grenoble Alpes (UGA)/ INSERM-U1209/CNRS-UMR 5309, 38700 Grenoble, France;* orcid.org/0000-0002-2453-3552; Email: jean-luc.coll@univ-grenoble-alpes.fr

Authors

Zhixi Yu − *Cancer Targets and Experimental Therapeutics, Institute for Advanced Biosciences (IAB), University of Grenoble Alpes (UGA)/ INSERM-U1209/CNRS-UMR 5309, 38700 Grenoble, France*

https://dx.doi.org/10.1021/acsnano.0c01174
ACS Nano 2020, 14, 4973−4981

Benjamin Musnier − *Cancer Targets and Experimental Therapeutics, Institute for Advanced Biosciences (IAB), University of Grenoble Alpes (UGA)/ INSERM-U1209/ CNRS-UMR 5309, 38700 Grenoble, France*
K. David Wegner − *BAM Federal Institute for Materials Research and Testing, 12489 Berlin, Germany*
Maxime Henry − *Cancer Targets and Experimental Therapeutics, Institute for Advanced Biosciences (IAB), University of Grenoble Alpes (UGA)/ INSERM-U1209/ CNRS-UMR 5309, 38700 Grenoble, France*
Benoit Chovelon − *Institut de Biologie et Pathologie, Centre Hospitalier Universitaire (CHU) de Grenoble Alpes, 38700 Grenoble, France*
Agnès Desroches-Castan − *Biology of Cancer and Infection Laboratory, University Grenoble Alpes, INSERM, CEA, 38000 Grenoble, France*
Arnold Fertin − *TIMC-IMAG Laboratory, University of Grenoble Alpes, CNRS-UMR 5525, 38700 Grenoble, France*
Ute Resch-Genger − *BAM Federal Institute for Materials Research and Testing, 12489 Berlin, Germany;* orcid.org/0000-0002-0944-1115
Sabine Bailly − *Biology of Cancer and Infection Laboratory, University Grenoble Alpes, INSERM, CEA, 38000 Grenoble, France*
Yves Usson − *TIMC-IMAG Laboratory, University of Grenoble Alpes, CNRS-UMR 5525, 38700 Grenoble, France*
Véronique Josserand − *Cancer Targets and Experimental Therapeutics, Institute for Advanced Biosciences (IAB), University of Grenoble Alpes (UGA)/ INSERM-U1209/ CNRS-UMR 5309, 38700 Grenoble, France*

Complete contact information is available at: https://pubs.acs.org/10.1021/acsnano.0c01174

Notes

The authors declare no competing financial interest.

ACKNOWLEDGMENTS

X.L.G. would like to thank Ines Häusler for the electron microscopy images (the TEM images were carried out as part of the DFG core facility project "Berlin Electron Microscopy Network (Berlin EM Network)") and Muriel Jourdan for the NMR measurements. X.L.G. would like to thank Cancéropôle Lyon Auvergne Rhône-Alpes (CLARA), Plan Cancer (C18038CS), and ARC (R17157CC) for their financial support. K.D.W. acknowledges the European Union's Horizon 2020 research and innovation program under the Marie Sklodowska-Curie grant agreement no. 846764. U.R.-G. aknowledges financial support from the German Research Council (DFG; RE1203/12-3). This research was funded by the Institut National de la Santé et de la Recherche Médicale (INSERM, U1036), the Commissariat à l'Energie Atomique et aux Energies Alternatives (CEA, DRF/IRIG), the University Grenoble Alpes (UGA, BCI), the Fondation pour la Recherche Médicale (FRM), the Agence Nationale de la Recherche (ANR grant no. ANR-17-CE14-0006; Be9inPAH), and the Labex GRAL (ANR-10-LABX-49-01 grant financed within the University Grenoble Alpes graduate school (Ecoles Universitaires de Recherche) CBH-EUR-GS (ANR-17-EURE-0003). All applicable international, national, and/or institutional guidelines for the care and use of animals were followed.

REFERENCES

(1) Hong, G.; Antaris, A.; Dai, H. Near-Infrared Fluorophores for Biomedical Imaging. *Nat. Biom. Eng.* **2017**, *1*, 0010.
(2) Hong, G.; Diao, S.; Chang, J.; Antaris, A. L.; Chen, C.; Zhang, B.; Zhao, S.; Atochin, D. N.; Huang, P. L.; Andreasson, K. I.; Kuo, C. J.; Dai, H. Through-Skull Fluorescence Imaging of the Brain in a New Near-Infrared Window. *Nat. Photonics* **2014**, *8*, 723−730.
(3) Hong, G.; Lee, J. C.; Robinson, J. T.; Raaz, U.; Xie, L.; Huang, N. F.; Cooke, J. P.; Dai, H. Multifunctional *In Vivo* Vascular Imaging Using Near-Infrared II Fluorescence. *Nat. Med.* **2012**, *18*, 1841−1846.
(4) Bruns, O.; Bischof, T.; Harris, D.; Franke, D.; Shi, Y.; Riedemann, L.; Bartelt, A.; Jaworski, F.; Carr, J.; Rowlands, C.; Wilson, M.; Chen, O.; Wei, H.; Hwang, G.; Montana, D.; Coropceanu, I.; Achorn, O.; Kloepper, J.; Heeren, J.; So, P.; Fukumura, D.; Jensen, K.; Jain, R.; Bawendi, M. Next-Generation *In Vivo* Optical Imaging with Shortwave Infrared Quantum Dots. *Nat. Biom. Eng.* **2017**, *1*, 0056.
(5) Zhong, Y.; Ma, Z.; Wang, F.; Wang, X.; Yang, Y.; Liu, Y.; Zhao, X.; Li, J.; Du, H.; Zhang, M.; Cui, Q.; Zhu, S.; Sun, Q.; Wan, H.; Tian, Y.; Liu, Q.; Wang, W.; Garcia, K. C.; Dai, H. *In Vivo* Molecular Imaging for Immunotherapy Using Ultra-Bright Near-Infrared-IIb Rare-Earth Nanoparticles. *Nat. Biotechnol.* **2019**, *37*, 1322−1331.
(6) Yang, Q.; Ma, Z.; Wang, H.; Zhou, B.; Zhu, S.; Zhong, Y.; Wang, J.; Wan, H.; Antaris, A.; Ma, R.; Zhang, X.; Yang, J.; Zhang, X.; Sun, H.; Liu, W.; Liang, Y.; Dai, H. Rational Design of Molecular Fluorophores for Biological Imaging in the Nir-II Window. *Adv. Mater.* **2017**, *29*, 1605497.
(7) Porret, E.; Le Guével, X.; Coll, J.-L. Gold Nanoclusters for Biomedical Applications: Toward *In Vivo* Studies. *J. Mater. Chem. B* **2020**, *8*, 2216−2232.
(8) Chen, Y.; Montana, D.; Wei, H.; Cordero, J.; Schneider, M.; Le Guevel, X.; Chen, O.; Bruns, O.; Bawendi, M. Shortwave Infrared *In Vivo* Imaging with Gold Nanoclusters. *Nano Lett.* **2017**, *17*, 6330−6334.
(9) Desroches-Castan, A.; Tillet, E.; Ricard, N.; Ouarné, M.; Mallet, C.; Feige, J.-J.; Bailly, S. Differential Consequences of Bmp9 Deletion on Sinusoidal Endothelial Cell Differentiation and Liver Fibrosis in 129/Ola and C57bl/6 Mice. *Cells* **2019**, *8*, 1079.
(10) Desroches-Castan, A.; Tillet, E.; Ricard, N.; Ouarné, M.; Mallet, C.; Belmudes, L.; Couté, Y.; Boillot, O.; Scoazec, J.-Y.; Bailly, S.; Feige, J.-J. Bone Morphogenetic Protein 9 Is a Paracrine Factor Controlling Liver Sinusoidal Endothelial Cell Fenestration and Protecting Against Hepatic Fibrosis. *Hepatology* **2019**, *70*, 1392−1408.
(11) Musnier, B.; Wegner, K. D.; Comby-Zerbino, C.; Trouillet, V.; Jourdan, M.; Hausler, I.; Antoine, R.; Coll, J. L.; Resch-Genger, U.; Le Guevel, X. High Photoluminescence of Shortwave Infrared-Emitting Anisotropic Surface Charged Gold Nanoclusters. *Nanoscale* **2019**, *11*, 12092−12096.
(12) Le Guevel, X.; Henry, M.; Motto-Ros, V.; Longo, E.; Montanez, M. I.; Pelascini, F.; de La Rochefoucauld, O.; Zeitoun, P.; Coll, J. L.; Josserand, V.; Sancey, L. Elemental and Optical Imaging Evaluation of Zwitterionic Gold Nanoclusters in Glioblastoma Mouse Models. *Nanoscale* **2018**, *10*, 18657−18664.
(13) Shen, D.; Henry, M.; Trouillet, V.; Comby-Zerbino, C.; Bertorelle, F.; Sancey, L.; Antoine, R.; Coll, J. L.; Josserand, V.; Le Guével, X. Zwitterion Functionalized Gold Nanoclusters for Multimodal Near Infrared Fluorescence and Photoacoustic Imaging. *APL Mater.* **2017**, *5*, 053404.
(14) Liu, H.; Hong, G.; Luo, Z.; Chen, J.; Chang, J.; Gong, M.; He, H.; Yang, J.; Yuan, X.; Li, L.; Mu, X.; Wang, J.; Mi, W.; Luo, J.; Xie, J.; Zhang, X.-D. Atomic-Precision Gold Clusters for Nir-II Imaging. *Adv. Mater.* **2019**, *31*, 1901015.
(15) Carr, J. A.; Franke, D.; Caram, J. R.; Perkinson, C. F.; Saif, M.; Askoxylakis, V.; Datta, M.; Fukumura, D.; Jain, R. K.; Bawendi, M. G.; Bruns, O. T. Shortwave Infrared Fluorescence Imaging with the Clinically Approved Near-Infrared Dye Indocyanine Green. *Proc. Natl. Acad. Sci. U. S. A.* **2018**, *115*, 4465−4470.

(16) Du, B.; Jiang, X.; Das, A.; Zhou, Q.; Yu, M.; Jin, R.; Zheng, J. Glomerular Barrier Behaves as an Atomically Precise Bandpass Filter in a Sub-Nanometre Regime. *Nat. Nanotechnol.* **2017**, *12*, 1096−1102.
(17) Tang, S.; Peng, C.; Xu, J.; Du, B.; Wang, Q.; Vinluan, R. D., Iii; Yu, M.; Kim, M. J.; Zheng, J. Tailoring Renal Clearance and Tumor Targeting of Ultrasmall Metal Nanoparticles with Particle Density. *Angew. Chem., Int. Ed.* **2016**, *55*, 16039−16043.
(18) Tillet, E.; Bailly, S. Emerging Roles of Bmp9 and Bmp10 in Hereditary Hemorrhagic Telangiectasia. *Front. Genet.* **2015**, *5*, 456.
(19) Levet, S.; Ciais, D.; Merdzhanova, G.; Mallet, C.; Zimmers, T. A.; Lee, S.-J.; Navarro, F. P.; Texier, I.; Feige, J.-J.; Bailly, S.; Vittet, D. Bone Morphogenetic Protein 9 (Bmp9) Controls Lymphatic Vessel Maturation and Valve Formation. *Blood* **2013**, *122*, 598−607.
(20) Frieden, B. R.; Zoltani, C. K. Monte Carlo Restoration of Binary Objects. *J. Opt. Soc. Am. A* **1986**, *3*, 731−734.
(21) Colicchio, B.; Xu, C.; Haeberlé, O.; Dieterlen, A.; Jacquey, S. Monte-carlo reconstruction of images from a psf variant system. Focus on Microscopy 2002, Kaohsiung (Taiwan), April 7−10, 2002, *Technical Digest of Focus on Microscopy* 2002, p. 56.
(22) Frangi, A. F.; Niessen, W. J.; Vincken, K. L.; Viergever, M. A. In *Multiscale Vessel Enhancement Filtering, Medical Image Computing and Computer-Assisted Intervention — MICCAI'98*; Wells, W. M., Colchester, A., Delp, S., Eds.; Springer Berlin Heidelberg: Berlin, Heidelberg, 1998; pp 130−137.
(23) Soleilhac, A.; Bertorelle, F.; Comby-Zerbino, C.; Chirot, F.; Calin, N.; Dugourd, P.; Antoine, R. Size Characterization of Glutathione-Protected Gold Nanoclusters in the Solid, Liquid and Gas Phases. *J. Phys. Chem. C* **2017**, *121*, 27733−27740.

https://dx.doi.org/10.1021/acsnano.0c01174
ACS Nano 2020, 14, 4973−4981